Full Text View

Volume 32, Issue 11 (November 2002)

Journal of Physical Oceanography
Article: pp. 3216–3232 | Abstract | PDF (1.67M)

Remote Topographic Forcing of a Baroclinic Western Boundary Current: An Explanation for the Southland Current and the Pathway of the Subtropical Front East of New Zealand*

Charles E. Tilburg+

Center for Ocean–Atmospheric Prediction Studies, The Florida State University, Tallahassee, Florida

Harley E. Hurlburt

Naval Research Laboratory, NASA John C. Stennis Space Center, Stennis Space Center, Mississippi

James J. O'Brien

Center for Ocean–Atmospheric Prediction Studies, The Florida State University, Tallahassee, Florida

Jay F. Shriver

Naval Research Laboratory, NASA John C. Stennis Space Center, Stennis Space Center, Mississippi

(Manuscript received May 9, 2001, in final form May 3, 2002)
DOI: 10.1175/1520-0485(2002)032<3216:RTFOAB>2.0.CO;2

ABSTRACT

The Southland Current is a western boundary current adjacent to the South Island of New Zealand and flows along a segment of the Southern Hemisphere subtropical front (STF). The physical mechanisms that govern the behavior of this current and other portions of the STF and subantarctic front (SAF) are investigated using one regional and three global ocean simulations. The three global ocean simulations used in this study are a 1½-layer reduced-gravity linear simulation, a six-layer nonlinear flat-bottom simulation, and a six-layer nonlinear simulation that incorporates vertically compressed, but otherwise realistic, bottom topography confined to the abyssal layer. All three simulations have horizontal spacings of 1/8° and are forced with climatological-mean monthly wind stress data. The regional simulation has a horizontal spacing of ½° and contains two layers, with an idealized bottom topography. The only forcing is supplied by inflow and outflow ports. The pathway of the SAF is shown to be strongly influenced by a barotropic response of the associated flow to bottom topography. Currents associated with the SAF flow along the southern edge of the Campbell Plateau, a large submarine platform southeast of New Zealand. In contrast, the location of the Southland Current and the pathway of the STF east of New Zealand are due to remote forcing of upper-ocean currents by topographically constrained abyssal currents. Whereas most western boundary currents can be described as responses of the ocean to interior Sverdrup flow with some modification, analysis of the numerical simulations within this study shows that the Southland Current is due to a completely different formation

Table of Contents:
- Introduction
- The model
- Topographic steering
- A two-layer illustration
- Summary and conclusions
- REFERENCES
- APPENDIX
- TABLES
- FIGURES

- Harley E. Hurlburt
- James J. O'Brien
- Jay F. Shriver

mechanism. The presence of the Southland Current and the STF east of New Zealand are instead due to a combination of northward topographic steering of surface-layer thickness gradients approximately 12° east of New Zealand and westward propagation of these perturbed gradients. A portion of the abyssal flow associated with the SAF is shown to form a topographically constrained deep western boundary current (DWBC). This DWBC follows the edge of the Campbell Plateau, eventually flowing generally northward. When the surface zonal flow associated with the STF southeast of New Zealand encounters this meridional abyssal flow, it is advected northward, creating an imbalance in the potential vorticity within the flow. In an attempt to conserve potential vorticity, the perturbed surface-layer thickness gradients propagate westward until they encounter New Zealand's South Island, at which point they form the observed Southland Current. Transport associated with the STF thus flows northward along South Island, eastward along the Chatham Rise, and southward once east of the rise. This formation mechanism and the downstream behavior of the STF are illustrated in a simplified regional simulation that reproduces the pathway of the STF and the location of the western boundary current extremely well.

1. Introduction

The Southern Ocean is characterized by a series of circumpolar fronts or abrupt changes in temperature and/or salinity that are associated with strong flow (e.g., Gordon 1975; Rintoul and Bullister 1999; Philips and Rintoul 2000). For two of these fronts, the subtropical front (STF) and the subantarctic front (SAF), the dynamics governing their pathways near New Zealand are investigated using one regional and three global ocean simulations. A portion of the flow associated with the STF forms the Southland Current, a baroclinic western boundary current along the east coast of New Zealand's South Island. Although the location and direction of most western baroclinic boundary currents can be described as a result of Sverdrup (1947) flow in the interior or some modification of it, the Southland Current is an example of a western boundary current with a discretely different formation mechanism. The presence of the Southland Current along the coast of South Island is due to remote forcing from strong topographically constrained abyssal currents located approximately 12° east of New Zealand. The pathways of several fronts within the Southern Ocean (including the SAF) are steered by barotropic responses to bottom topography. In contrast, the northward migration of the baroclinic STF east of New Zealand and related formation of the Southland Current are due to a unique combination of northward advection of upper-layer thickness gradients by a topographically constrained abyssal current and westward propagation of these gradients.

A regional schematic of the flow field superimposed on the bottom topography (Fig. 1) depicts two primarily zonal fronts, the STF and the SAF, south of New Zealand along with a deep western boundary current (DWBC). The SAF (white line in Fig. 1) is associated with the 8°–8.5°C isotherms in an annual mean of sea surface temperature (SST; Fig. 2) compiled by Uddstrom and Oien (1999) and is located between 50° and 56°S, skirting the southern edge of the Campbell Plateau before continuing eastward. The STF (gray line in Fig. 1) extends northward along the east coast of South Island (Chiswell 1996; Stramma et al. 1995), eastward along the Chatham Rise, and southward to 47°S beyond 177°W (Uddstrom and Oien 1999). The Southland Current, the northeastward boundary current adjacent to New Zealand's South Island, is associated with the northward extension of the STF. The transport of relatively cold water by the Southland Current along the east coast of South Island has a profound effect on South Island, providing a significantly colder climate than that of North Island (Salinger 1979). The composition of the STF is more complex than the SAF and is not represented by a single set of observed isotherms. West of New Zealand, the STF is associated with the 12°–13°C isotherms while directly east of New Zealand the Southland Current contains a significant amount of 11°C water. The southward dip of the STF at 53°S, 173°W is evident in the observed 9°–9.5°C isotherms. The DWBC (transparent line in Fig. 1) is associated with the SAF south of New Zealand and is constrained to follow f/h contours (see appendix for definitions of all variables) along the eastern edges of the Campbell Plateau, the Chatham Rise, and the Kermadec Ridge (Carter and Wilkin 1999; Warren 1981); however, a portion of the DWBC separates from the Campbell Plateau and continues eastward onto the abyssal plain.

There have been several previous numerical studies of this region, including two comprehensive studies of the abyssal flow; however, these studies did not focus on the dynamics that govern the behavior of the two fronts and the Southland Current. Bye et al. (1979), using a diagnostic linear regional model driven by specified density, wind stress, and flow boundaries, obtained a steady-state flow field around New Zealand, reproducing the Southland Current. Semtner and Chervin (1992) briefly examined this region in the analysis of their ½° 20-level global model that incorporated realistic bottom topography and was driven by climatological monthly wind stress data. Examination of the mean flow fields southeast of New Zealand revealed barotropic currents associated with fronts that followed f/h contours, resulting in an unrealistic depiction of the STF. Moore and Wilkin (1998) examined the variability of the South Pacific DWBC using the 0.28° 20-level Los Alamos National Laboratories (LANL) global model forced with daily wind stresses and current-meter observations north of New Zealand and east of the Kermadec Ridge. Carter and Wilkin (1999) examined the abyssal circulation along the eastern edge of the Campbell Plateau, the Chatham Rise, and the Kermadec Ridge by comparing the DWBC simulated by the LANL model to a suite of hydrographic measurements and geological proxies. From limited observations, they were able to make estimates of the location, direction, and magnitude of the DWBC.

Tilburg et al. (2001), using a model identical to that used in this study, found that simulations incorporating bottom topography were able to reproduce the observed Southland Current and the pathways of the SAF and STF but flat-bottom simulations and reduced-gravity simulations were not. They concluded that the location of the Southland Current was governed by bottom topography but did not discuss the mechanism responsible.

This earlier work is extended through the use of an isopycnal ocean model to examine the dynamics governing the Southland Current and the pathways of the Southern Hemisphere STF and the SAF near New Zealand. Because flow associated with the STF, SAF, and DWBC is situated in one of the most diverse and interconnected regions of the world's oceans and is influenced by the Antarctic Circumpolar Current (ACC), the Indo-Pacific Throughflow, and the global thermohaline circulation, global simulations are first used to capture the range of essential dynamics. The ocean model is used in three different global configurations to analyze the flow field: a reduced-gravity linear simulation, a flat-bottom nonlinear simulation, and a nonlinear simulation with realistic bottom topography. Next, an idealized configuration of the same model is used to produce a regional simulation to isolate and illustrate the dynamics governing the behavior of the Southland Current and the STF. The model used in this investigation is discussed in section 2. The results and dynamical interpretation of the different global simulations are discussed in section 3. The idealized two-layer simulation is discussed in section 4, followed by a summary and conclusions in section 5.

2. The model

The numerical model used for all simulations in this investigation is the Naval Research Laboratory Layered Ocean Model (NLOM), a primitive equation layered formulation whose equations have been integrated through each layer. This model is a descendent of the model initially described by Hurlburt and Thompson (1980) with greatly expanded capabilities (Wallcraft 1991; Wallcraft and Moore 1997; Moore and Wallcraft 1998). The equations for the n-layer finite-depth, hydrodynamic model are given below for layers $k = 1, \ldots, n$ with $k = 1$ for the top layer (in places where k is used to index model interfaces, $k = 0$ is the surface and $k = n$ is the bottom):

$$\frac{\partial U_k}{\partial t} + \frac{1}{a\cos\theta}\left[\frac{\partial(U_k u_k)}{\partial\phi} + \frac{\partial(V_k u_k \cos\theta)}{\partial\theta} - V_k(u_k \sin\theta + a\Omega \sin 2\theta)\right]$$
$$= \max(0, -\omega_{k-1})u_{k-1} + \max(0, \omega_k)u_{k+1} - [\max(0, -\omega_k) + \max(0, \omega_{k-1})]u_k + \max(0, -C_M\omega_{k-1})(u_{k-1} - u_k)$$
$$+ \max(0, C_M\omega_k)(u_{k+1} - u_k) - \frac{h_k}{a\cos\theta}\sum_{j=1}^{n} G_{kj}\frac{\partial(h_j - H_j)}{\partial\phi} + \frac{(\tau_{\phi_{k-1}} - \tau_{\phi_k})}{\rho_0}$$
$$+ \frac{A}{a^2\cos^2\theta}\left[\frac{\partial(h_k e_{\phi\phi_k}\cos\theta}{\partial\phi} + \frac{\partial(h_k e_{\phi\theta_k}\cos^2\theta}{\partial\theta}\right], \tag{1}$$

$$\frac{\partial V_k}{\partial t} + \frac{1}{a\cos\theta}\left[\frac{\partial(U_k v_k)}{\partial\phi} + \frac{\partial(V_k v_k \cos\theta)}{\partial\theta} + U_k(u_k \sin\theta + a\Omega \sin 2\theta)\right]$$
$$= \max(0, -\omega_{k-1})v_{k-1} + \max(0, \omega_k)v_{k+1} - [\max(0, -\omega_k) + \max(0, \omega_{k-1})]v_k + \max(0, -C_M\omega_{k-1})(v_{k-1} - v_k)$$
$$+ \max(0, C_M\omega_k)(v_{k+1} - v_k) - \frac{h_k}{a}\sum_{j=1}^{n} G_{kj}\frac{\partial(h_j - H_j)}{\partial\theta} + \frac{(\tau_{\theta_{k-1}} - \tau_{\theta_k})}{\rho_0}$$
$$+ \frac{A}{a^2\cos^2\theta}\left[\frac{\partial(h_k e_{\phi\theta_k}\cos\theta)}{\partial\phi} + \frac{\partial(h_k e_{\theta\theta_k}\cos^2\theta)}{\partial\theta}\right], \quad \text{and} \tag{2}$$

$$\frac{\partial h_k}{\partial t} + \nabla\cdot\mathbf{V}_k = \omega_k - \omega_{k-1}. \tag{3}$$

(Click the equation graphic to enlarge/reduce size)

Although notation that is common in oceanography is used in the model equations, an explanation of the parameters and notation is given in the appendix. The model boundary conditions are kinematic and no slip.

Although thermodynamic versions of the model exist (Metzger et al. 1992; Heburn 1994; Metzger and Hurlburt 1996), including versions with a mixed layer and sea surface temperature (Rochford et al. 2000; Wallcraft et al. 2002, manuscript submitted to *J. Atmos. Oceanic Technol.*), the versions used in this investigation are hydrodynamic with constant density in each layer. As a result, thermal forcing and steric anomalies due to seasonal heating and cooling are excluded. The model does permit isopycnal outcropping via ventilation of model layer interfaces, allowing overturning circulations in the vertical, such as the thermohaline circulation and meridional overturning.

A modified version of the 1/12° "ETOP05" bottom topography (National Oceanic and Atmospheric Administration 1986) is used in the simulation that requires realistic bottom topography. The topography is first interpolated to the model grid and then smoothed two times with a nine-point smoother to reduce energy generation at smaller scales that are poorly resolved by the model. The maximum depth of the model is set at 6500 m. The minimum depth, set at 200 m, is used as the model boundary with a few exceptions where shallower depths are needed to connect semienclosed seas. The bottom topography is confined to the lowest layer (Hurlburt and Thompson 1980) by multiplying all topography relative to 6500 m by 0.65. This compression prevents numerical difficulties that arise when moving layer interfaces intersect with sloping topography and greatly decreases the computer time/model year. The flow through shallow straits is constrained to small values below the sill depth. Two of the main reasons for including bottom topography, regulating baroclinic instabilities and forcing abyssal flow to follow f/h contours, are relatively unaffected by this modification of the bottom topography.

The simulations used in this investigation are defined in Table 1, and the model parameters are given in Tables 1 and 2. The density for each layer of the six-layer nonlinear simulations was obtained from the Levitus (1982) ocean climatology. The depths of the two upper layers were chosen to represent a surface layer and a layer containing the equatorial undercurrent, and the mean fifth interface depth was chosen to represent the boundary between intermediate and abyssal water. The global simulations have horizontal spacings of 1/8°, are forced by the Hellerman and Rosenstein (1983) monthly wind stress climatology to statistical equilibration, and are initialized from equilibrated lower-resolution simulations. All means shown are calculated from the last four years of the simulation. Numerous model–data comparisons have shown that five- and six-layer global and basin-scale simulations using NLOM are able to successfully reproduce the Gulf Stream (Hurlburt and Hogan 2000) and features in the Pacific Ocean such as the Kuroshio (e.g. Hurlburt et al. 1996; Mitchell et al. 1996). Other studies have used variations of the model to investigate the effects of bottom topography on the flow north of New Zealand (Tilburg et al. 2001) and the Kuroshio bifurcation (Metzger and Hurlburt 1998), the effects of the Indo-Pacific Throughflow on the global thermohaline circulation (Shriver and Hurlburt 1997), and the role of Halmahera Island in the transport pathways of Pacific waters to the Indian Ocean (Morey et al. 1999). Although not the case for all applications and locations—for example, detailed examination of the bottom boundary layer or the vertical structure of the meridional overturning within that thick layer—representation of the abyssal layer as one vertically integrated layer has been shown to be effective in the analysis of abyssal flows and bottom steering of surface currents by those flows. Flow in the abyssal layer of five- and six-layer simulations using NLOM has been compared with observations of abyssal eddy kinetic energy (EKE) across the Kuroshio (Hurlburt et al. 1996) and abyssal transport and EKE in the subtropical Atlantic (Hurlburt and Hogan 2000), with generally favorable results. The current study uses a similar version of NLOM configured for a nearly global domain. Some of the earlier studies used lower resolution; others required higher resolution to represent certain phenomena. The regional two-layer simulation also uses NLOM but in an idealized representation of the South Pacific Ocean east of New Zealand. It has a horizontal spacing of ½° and consists of a rectangular domain with an inflow and outflow port in each layer to simulate the flow associated with the STF and the DWBC.

3. Topographic steering of the surface flow

To determine which dynamics govern the behavior of the Southland Current and the pathways of the STF and the SAF, we examine three simulations: a linear 1½-layer reduced-gravity global simulation (hereinafter called RG), a six-layer nonlinear global simulation with a flat bottom (FB), and a six-layer nonlinear global simulation with realistic bottom topography (RBa). The three simulations have a horizontal grid spacing of 1/8° and are forced by climatological-mean monthly wind stress. They represent a systematic increase in complexity and realism in the model. Because there are significant transports associated with the STF and SAF (e.g., Gille 1994; Philips and Rintoul 2000), hydrodynamic simulations are able to reproduce the flow patterns within our region of interest. However, the fronts are no longer identified by sharp gradients in temperature as shown in Fig. 2, but instead as gradients in sea surface height (SSH) and layer interface depth. The following analysis shows that the pathways of the fronts are governed not by the Sverdrup (1947) response of the ocean to wind stress, but instead by the interaction of the bottom topography and the flow fields associated with the fronts.

The lowest-order estimate of the dynamics governing the flow southeast of New Zealand is the reduced-gravity linear simulation (RG) whose dynamics are essentially those of a Sverdrup (1947) interior with Munk (1950) western boundary layers and globally applied horizontal friction. The non-Sverdrup ACC in RG is constrained to realistic transport values by increased friction patches in the Drake Passage. A 4-yr mean of the SSH deviation field from RG (Fig. 3) reveals that while some large-scale features are adequately described by linear dynamics the Southland Current and the fronts are not. The East Australian Current separates from the coast of Australia at the observed latitude (~ 32°–33°S), and the southern portion of the Southern Hemisphere subtropical gyre is realistically portrayed in the model. However, there is no evidence of a northward-flowing Southland Current along the east coast of South Island as seen in Fig. 2; instead linear dynamics dictate that there should be a *southward* flow along the coast. Also, there is no evidence of fronts within the Southern Ocean; instead it is characterized by a uniform zonal flow. It is clear that the Southland Current and the pathways of the STF and the SAF are not due to the direct linear response of the ocean to wind stress. A nonlinear modification of the Sverdrup (1947) response can also be dismissed. Tilburg et al. (2001), using simulations identical to this study, showed that the introduction of nonlinearities and vertical structure to the model results in strong southward flow along the eastern coast of North Island. A nonlinear modification of the linear flow field found in RG (Fig. 3) to incorporate these stronger southward flows would tend to intensify, not reverse, the unrealistic southward-flowing Southland Current, as demonstrated in Tilburg et al. (2001).

The flow field is next examined using the two nonlinear configurations (FB and RBa) of the model, which differ only in their choice of bottom topography and small deviations in the initial stratification. Comparison of the two simulations allows the direct examination of the impact of bottom topography on the surface flow field. Four-year means of SSH deviations from FB (Fig. 4a) and RBa (Fig. 4b) reveal that the addition of nonlinearities and vertical structure does result in fronts within the Southern Ocean. (Again, because the simulations are hydrodynamic, the simulated fronts corresponding to the STF and SAF identified in Fig. 2 are characterized by sharp gradients in SSH, not temperature.) SSH deviation contours that are representative of the examined fronts are marked in red (STF) and green (SAF) in Fig. 4. Examination of these fields reveals that, although the flat-bottom simulation, FB, does contain fronts southeast of New Zealand, it fails to reproduce the observed Southland Current or the observed meridional deviations of the fronts and instead produces nearly zonal flow at all latitudes southeast of New Zealand. RBa, however, produces realistic portrayals of the Southland Current, the STF, and the SAF.

Observations of the abyssal and surface currents associated with the STF and SAF indicate that the flow fields within the two fronts contain extremely different vertical profiles. Rintoul and Bullister (1999), examining a hydrographic section

between Tasmania and Antarctica, found that sloping isopycnals associated with the STF corresponding to eastward flow were limited to the upper 600 dbar, whereas those of the SAF extended to the ocean floor. Philips and Rintoul (2000), examining current meters near 50.5°S, 143°E, also observed relatively strong abyssal flow associated with the SAF. In a much earlier study, Gordon (1975), using current meters placed 100 meters above the seafloor, recorded an eastward velocity of 29 cm s^{-1} at approximately 5000 m at 56°S, 170°E, directly south of the Campbell Plateau. This observed vertical structure of the flow associated with these fronts is represented well in both simulations. The baroclinic nature of the STF appears within FB as an eastward surface flow (red line in Fig. 5a) and a westward abyssal flow (red line in Fig. 5b) west of New Zealand. Within RBa, there are strong eastward surface currents (red line in Fig. 6a) but no significant abyssal currents (red line in Fig. 6b) associated with the STF directly east or west of New Zealand. Both simulations reproduce flow associated with the SAF (green lines in Figs. 5 and 6) that extends to the abyssal layer.

The physical mechanism responsible for the pathway of the SAF is relatively straightforward, and we begin with its discussion. The pathway is governed by conservation of potential vorticity, a sufficient constraint to allow even deep low-amplitude topographic features to steer the abyssal flow. The high vertical coherence of the flow within this front results in abyssal and surface currents that closely follow topographic features south of New Zealand. In the simulation with a flat bottom, the surface currents (Fig. 5a) and abyssal currents (Fig. 5b) associated with the SAF are zonal south of New Zealand. However, with the addition of realistic bottom topography, the abyssal currents are constrained to follow f/h contours dictated by the topography. Within RBa, abyssal currents (Fig. 6b) associated with the SAF flow eastward along a complicated pathway over the relatively flat southern edge of the Tasman Sea, but at ~160°E they encounter the Macquarie Ridge. The abyssal flow enters the Emerald Basin through gaps in the Ridge (Fig. 2) and flows along the eastern edge of the ridge until it encounters the Campbell Plateau. There, it turns southward and then northward following the edge of the plateau, forming the DWBC (Fig. 6b) described by Moore and Wilkin (1998) and Carter and Wilkin (1999). The barotropic nature of the flow results in a similar pathway for the surface currents evident in both the simulation (Fig. 6a, green line) and in observations of SST (Fig. 2, 8°–8.5°C isotherms). The surface flow associated with the SAF follows a southward meander at ~148°E (also seen in the abyssal flow) before it continues eastward to ~160°E, where it turns northward upon encountering the Macquarie Ridge and follows the edge of the Campbell Plateau. This barotropic behavior of Southern Ocean fronts has been noted before (e.g. Gille 1994; Uddstrom and Oien 1999). When the flow reaches the same latitude as before it encountered Macquarie Ridge (~52°–54°S, 180°), the surface flow separates from the plateau and continues along an eastward path. The abyssal flow bifurcates at this point. One portion of the abyssal flow separates from the plateau and continues eastward while the other portion proceeds northeastward along the eastern edge of the Campbell Plateau. In essence, the vertically coherent flow associated with the SAF encounters a change in bottom topography and flows around the obstacle to conserve potential vorticity.

The location of the Southland Current and the STF east of New Zealand are due to a unique interaction between the surface flow and the DWBC formed by the abyssal flow associated with the SAF. Inspection of the surface currents from FB (Fig. 5a) shows no indication of a realistic western boundary current or realistic pathway of the STF; instead the simulated STF is zonal, as is the SAF. However, examination of the surface currents associated with the STF in RBa (Fig. 6a) reveals an eastward baroclinic flow south of New Zealand that turns northeastward along the east coast of South Island, eastward near the Chatham Rise, and southward near 175°W. The pathways of the Southland Current and the STF within RBa (Fig. 6a, red line) agree well with observations (Fig. 2). The simulated transport of the Southland Current also agrees well with the limited observations. Chiswell (1996) estimated the geostrophic transport of the Southland Current relative to 1000 dbar to be 10.4 Sv (1 Sv $\equiv 10^6$ m^3 s^{-1}). Although he states that this value could be subject to large errors, the simulated mean transport from RBa at the same location is 11.0 Sv relative to 1100 m, providing remarkably good agreement between the model and observations. In contrast, the DWBC is underestimated by RBa, which has a simulated mean transport of 12.4 Sv, somewhat less than the 20 Sv observed by Warren (1973, 1976).

Comparison of results from RBa and FB demonstrates that the location and direction of the Southland Current and the STF are strongly influenced by the bottom topography. However, the Southland Current and flow within the entire STF are strongly baroclinic, with no indication of a corresponding abyssal flow (Fig. 6b). The formation of both the western boundary current and the downstream path of the STF is not due to a barotropic response of the flow to bottom topography as is the SAF but is instead due to remote forcing resulting from the interaction of the surface flow with the DWBC along the Campbell Plateau. Topographically constrained abyssal currents like the DWBC have been shown to influence surface currents, such as those associated with the STF, that do not directly impinge on the topography. Hurlburt and Metzger (1998) found indications that the abyssal flow associated with the Shatsky Rise topography affects the bifurcation of the Kuroshio, and Tilburg et al. (2001) found evidence that the meridional abyssal flow associated with ridges and troughs creates meanders in the zonal Tasman Front. Hurlburt and Thompson (1980, 1982, 1984) used the continuity equation to explain the mechanism responsible for the influence of abyssal flow on surface currents. An abbreviated version of their explanation is presented here. In a layered model, the continuity equation for layer k can be written as

$$\frac{\partial h_k}{\partial t} + \mathbf{v}_k \cdot \nabla h_k + h_k \nabla \cdot \mathbf{v}_k = 0. \qquad (4)$$

For a two-layer system, the geostrophic component of the advection term within the layer-1 continuity equation can be linked to the layer-2 velocity by

$$\mathbf{v}_{1g} \cdot \nabla h_1 = \mathbf{v}_{2g} \cdot \nabla h_1 = (g/f) J(\eta_1, \eta_2), \quad (5)$$

where $\mathbf{v}_{kg}$ is the geostrophic velocity in layer k, J is the Jacobian operator, η_1 is the deviation of the free surface from its

initial value, and η_2 is the deviation of the interface between the two layers from its initial value. In physical terms, Eq. (5) states that, in a two-layer model, geostrophically balanced upper- and lower-layer currents advect upper-layer thickness gradients (∇h_1) in the same manner because $\mathbf{v}_{1g} - \mathbf{v}_{2g}$ is parallel to ∇h_1. This advection can be very large when a strongly tilted thermocline (such as that associated with the STF) intersects an intense deep flow (such as the DWBC). The ability of abyssal currents to advect surface currents can be seen by considering the geostrophic balance of the internal mode in the two-layer model:

$$\mathbf{k} \times f(\mathbf{v}_{1g} - \mathbf{v}_{2g}) = -g'\nabla h_1, \quad (6)$$

where $g' = g(\rho_2 - \rho_1)/\rho_0$. When the surface currents are much larger than the abyssal currents ($|\mathbf{v}_{1g}| \gg |\mathbf{v}_{2g}|$), which is typically the case in a two-layer model (and is the case for the currents associated with the STF and the DWBC), Eq. (6) indicates that ∇h_1 can be used as an approximate measure of $\mathbf{v}_{1g}$. From this observation and consideration of Eqs. (5) and (6), we see that the abyssal currents can advect upper-layer thickness gradients and, therefore, steer upper-layer currents. Hurlburt et al. (1996) showed that, although this theory formally breaks down in the multilayer case, this steering effect remains when the first baroclinic and barotropic modes dominate the flow regime. Tilburg (2000) performed a normal mode analysis of selected flow fields associated with the STF east of New Zealand and south of the Chatham Rise. As discussed in Tilburg (2000) and Tilburg et al. (2001), this analysis showed that the barotropic and first baroclinic modes do indeed dominate the flow fields and that the steering mechanism is possible in this region.

Comparison of simulations RBa and FB allows the direct examination of the effect of the presence and absence of the DWBC on the location of the STF. The flat-bottom simulation (no DWBC) shows an STF position east of New Zealand consistent with the dictates of the wind stress curl field. This can be seen by comparing simulations FB (Fig. 4a) and RG (Fig. 3). The topographically constrained meridional DWBC in RBa (Fig. 6b) provides the necessary northward advection for an STF that would otherwise be nearly zonal. However, the surface flow field of RBa (Fig. 6a) reveals that the northward current segment associated with the STF is not adjacent to the DWBC but instead has propagated westward to form a western boundary current, the Southland Current, along the east coast of New Zealand. The evolution of the STF can be explained as a two-part process: first meridional advection and then westward propagation of the front. As the surface zonal flow associated with the STF encounters the meridional abyssal flow of the DWBC at about 178°E, the surface flow is advected northward by the steering mechanism just discussed. The northward displacement of the flow associated with the STF creates an imbalance in potential vorticity. Because there is nothing to constrain the now meridional STF, the surface layer thickness gradients associated with it propagate westward in an attempt to conserve potential vorticity via the beta effect. This propagation continues until they encounter the east coast of South Island where they generate a western boundary current. Once the STF passes east of this meridional DWBC, it returns southward past the latitude seen in FB because of southward abyssal flow, including flow near 173°W (Fig. 6b), which occurs along the western side of a topographic depression (Fig. 1).

4. A two-layer illustration

The dynamics behind the formation of the Southland Current and the pathway of the STF are not immediately evident in the equilibrated simulation described above. However, they can be illustrated by examining a two-layer regional simulation (RBb) consisting of an initially zonal surface flow (representing the STF and the Southland Current) and an abyssal meridional flow (representing the DWBC). The domain of the simulation is rectangular with zonal (165°E–105°W) and meridional (55°–15°S) dimensions that roughly correspond to the South Pacific Ocean east of New Zealand. The horizontal spacing is ½°, and the boundary conditions are no slip and closed on all sides except for two ports in each layer. There is no wind forcing. Instead, the surface flow is forced by 2°-wide meridional ports in layer 1 centered at 45°S on the east and west boundaries. These ports correspond to flow south of New Zealand (western inflow port) and flow through the Drake Passage (eastern outflow port). The transport through the surface ports is specified to be 5 Sv, producing velocities (0.075 m s^{-1}) similar to the depth-averaged velocity of the top two layers of RBa (0.068 m s^{-1}). The abyssal currents are constrained to flow northward by a sharp gradient in bottom topography representing the eastern edge of the Campbell Plateau (Fig. 7) and are generated by 2°-wide zonal ports in layer 2 centered at 177°E on the northern (outflow) and southern (inflow) boundaries. The transport through the abyssal ports is specified to be 20 Sv, corresponding to estimated values of the DWBC at 28° and 43°S (Warren 1973, 1976). Although this transport is larger than that of RBa, it produces abyssal velocities (0.027 m s^{-1}) similar to those of RBa (0.029 m s^{-1}). Although the flow field has reached a statistical equilibrium in the global simulations, a transient simulation, in which a previously zonal surface flow is suddenly subjected to a meridional abyssal flow, is instructive in the illustration of the formation of the Southland Current and thus the nature of its equilibrated dynamics in the global simulations and real ocean. Several snapshots of the STF during the transient simulation illustrate the evolution from an initially zonal front through its meridional advection and westward propagation to its final observed location with the Southland Current along the western boundary.

The two-layer simulation consists of two parts: the spinup run and the temporal formation of the STF. First, the simulation is allowed to run until equilibrium (100 years) with a zonal surface flow but no abyssal flow (Fig. 8a). Because of the baroclinic nature of the flow, the surface flow field is unaffected by the change in topography and proceeds throughout the domain as a zonal flow. This equilibrium state is designated as $T = 0$ yr. At $T = 0$ yr, the meridional abyssal flow is turned on, which produces a meridional displacement of the surface flow, shown here at $T = 3$ yr (Fig. 8b). A snapshot of the flow field at $T = 7$ yr (Fig. 8c) shows the meridional structure has begun to propagate westward in an attempt to conserve potential vorticity. When this meridional flow encounters the western boundary, it forms a northward boundary current. At $T = 80$ yr, the end of the simulation, the surface flow has formed a strong western boundary current

(Fig. 8d) caused solely by the meridional abyssal flow 12° to the east. As the surface flow passes directly over the abyssal flow, it returns to its previous latitude because of the location of the outflow port, creating a pathway corresponding to that observed by Uddstrom and Oien (1999).

5. Summary and conclusions

Earlier studies have investigated the impact of topographically constrained abyssal currents on the pathways of upper-ocean currents that did not impinge on the topography (Hurlburt et al. 1996; Hurlburt and Metzger 1998; Hogan and Hurlburt 2000; Tilburg et al. 2001). In these studies, the impact was local to specific topographic features, and the abyssal currents were generally driven by mixed baroclinic–barotropic flow instabilities (which are not required for the DWBC in the present study). The present study differs in that the abyssal current (DWBC) has a remote impact that explains the existence and direction of a northward baroclinic western boundary current about 12° to the west: the Southland Current along the east coast of South Island, New Zealand. It also explains the northward displacement of the subtropical front east of New Zealand. It is noteworthy that the Southland Current is a western boundary current, which flows opposite to the direction predicted by Sverdrup flow and opposite to a second mechanism for southward flow along the east coast of New Zealand outlined by Tilburg et al. (2001).

One regional and three global ocean simulations are used to examine and illustrate the dynamics responsible for the formation of the Southland Current, as well as the pathways of the subtropical front and the subantarctic front, particularly east of New Zealand. The Southland Current flows along a segment of the STF. Although not all fronts are directly associated with strong flows, observations and numerical simulations have shown that both the STF and SAF are collocated with strong currents, allowing the use of hydrodynamic models in their examination. The global simulations used in this study have horizontal grid spacings of $^{1}/_{8}$° and range in dynamical complexity from a linear 1½-layer reduced-gravity simulation to a nonlinear six-layer flat-bottom simulation to a nonlinear six-layer simulation that contains realistic bottom topography. All three global simulations are forced by the Hellerman and Rosenstein (1983) climatological-mean monthly wind stress and were spun up to statistical equilibrium at ½° and ¼° spacings before continuing at $^{1}/_{8}$°. The regional simulation has a horizontal grid spacing of ½° and comprises two layers with an idealized bottom topography representing the Campbell Plateau. It is forced by flow through ports in the model boundaries rather than wind stress. Its role is to isolate and illustrate the dynamics responsible for the formation of the Southland Current and the northward displacement of the STF east of New Zealand.

Although most western boundary currents (such as the Gulf Stream, the Kuroshio, and the East Australian Current) can be described as modified results of the Sverdrup (1947) response of the ocean to the wind stress curl, the Southland Current is shown to be an example of a new formation mechanism for a baroclinic western boundary current: a unique combination of topographic steering and westward propagation. The linear reduced-gravity simulation produces a southward “Southland Current,” opposite to that observed. It also fails to produce a realistic STF or SAF east of New Zealand, demonstrating that the formation of this western boundary current and the pathways of the two fronts are not due to Sverdrup (1947) dynamics. A six-layer flat-bottom nonlinear simulation reproduces fronts that contain vertical flow structure similar to that of the observed SAF and STF but shows no evidence of their observed meridional structure. The flat-bottom simulation produces a baroclinic flow directly south of New Zealand (corresponding to the STF) and a more barotropic flow slightly farther south (corresponding to the SAF), but the flat bottom eliminates the observed northward DWBC, and the simulated surface flows are nearly zonal. A nonlinear simulation that incorporates realistic bottom topography reproduces the observed northward DWBC and meridional structure of the fronts, revealing that the behavior of the Southland Current and the pathways of the STF and the SAF are influenced by the presence of bottom topography.

The pathway of the SAF is shown to be influenced by a barotropic response of the associated flow field to bottom topography. Examination of the pathway shows that the flow is deflected northward along the Macquarie Ridge and then follows the southern edge of the Campbell Plateau. After a portion of the flow separates from the Plateau, it returns to the same latitude as before encountering the Macquarie Ridge. In essence, the vertically coherent flow associated with the SAF follows f/h contours around an obstacle in an attempt to conserve potential vorticity.

The physical mechanisms responsible for the location of the STF are considerably more complex, consisting of a combination of bottom steering of surface-layer thickness gradients by a strong DWBC and westward propagation of these perturbed gradients. The abyssal flow associated with the SAF bifurcates when the surface flow separates from the eastern edge of the Campbell Plateau, with a portion flowing eastward with the surface currents and a portion continuing northward along the eastern edge of the plateau as a DWBC. This meridional abyssal current advects surface-layer thickness gradients in the STF northward, which then propagate westward in an attempt to conserve potential vorticity. When they encounter the east coast of New Zealand, they form a baroclinic western boundary current, the Southland Current. The equilibrated result of this combination is a front with an accompanying flow field that proceeds northward along the eastern coast of South Island as a strongly baroclinic western boundary current, continues eastward along the Chatham Rise, and then returns southward east of the northward-flowing DWBC.

Because bottom steering is dominated by the first baroclinic mode, a simulation with only two layers, one representing surface flow and one representing abyssal flow, is able to reproduce the observed conditions. We use an idealized two-layer regional simulation to illustrate the evolution of a strictly zonal flow to that observed, solely as a result of the introduction of topographically constrained abyssal currents and westward propagation. An equilibrated eastward zonal surface-layer current (representing flow associated with the STF) is perturbed by introducing a northward abyssal flow (representing the DWBC) along a topographic slope (representing the eastern edge of the Campbell Plateau), which lies 12° east of the western boundary. A sequence of flow-field snapshots is used to illustrate this evolution. These demonstrate that when the

surface-layer thickness gradients associated with the zonal surface flow encounter the meridional abyssal flow, they are advected northward in the vicinity of the DWBC. This northward perturbation creates an imbalance in potential vorticity on the west side of the perturbation. The now meridional gradients propagate westward in an attempt to conserve potential vorticity until they encounter the western boundary of the domain. After a considerable adjustment time, the resulting steady-state flow agrees very well with both observations and the more complex global simulation, consisting of a northward flow along the western boundary, an eastward flow that crosses above the DWBC farther to the east, and a return flow to the original latitude east of the DWBC.

Acknowledgments

This work is a contribution to the 6.1 Project “Thermodynamic and Topographic Forcing in Global Ocean Models” sponsored by the Office of Naval Research under Program Element 601153N. The computations in this paper were performed on AHPCRC, ARSC, CEWES, and NAVO Cray T3Es using grants of computer time from the Defense Department High Performance Computing Modernization Office. Charles Tilburg received financial support for this work from the Department of Defense through a National Defense Science and Engineering Graduate Fellowship. The ONR Physical Oceanography Program provides a Secretary of the Navy Grant to Dr. James J. O'Brien as the base support for the Center for Ocean–Atmospheric Prediction Studies (COAPS). The model development work of Dr. Alan Wallcraft and the computational assistance of Joseph Metzger are noted and greatly appreciated.

REFERENCES

Bye J. A. T., R. A. Heath, and T. W. Sag, 1979: A numerical model of the oceanic circulation around New Zealand. *J. Phys. Oceanogr.*, **9**, 892–899. Find this article online

Carter L., and J. L. Wilkin, 1999: Abyssal circulation around New Zealand—A comparison between observations and a global circulation model. *Mar. Geol.*, **159**, 221–239. Find this article online

Chiswell S. M., 1996: Variability in the Southland Current, New Zealand. *N. Z. J. Mar. Freshwater Res.*, **30**, 1–17. Find this article online

Gille S. T., 1994: Mean sea surface height of the Antarctic Circumpolar Current from Geosat data: Method and application. *J. Geophys. Res.*, **99**, 18255–18273. Find this article online

Gordon A. L., 1975: An Antarctic oceanographic section along 170°E. *Deep-Sea Res.*, **22**, 357–377. Find this article online

Heburn G. W., 1994: The dynamics of the seasonal variability of the western Mediterranean circulation. *Seasonal and Interannual Variability of the Western Mediterranean Sea*, P. E. LaViolette, Ed., Coastal Estuarine Studies, Vol. 46, Amer. Geophys. Union, 249–285.

Hellerman S., and M. Rosenstein, 1983: Normal monthly wind stress over the world ocean with error estimates. *J. Phys. Oceanogr.*, **13**, 1093–1104. Find this article online

Hogan P. J., and H. E. Hurlburt, 2000: Impact of upper ocean–topographical coupling and isopycnal outcropping in Japan/East Sea models with 1/8° to 1/64° resolution. *J. Phys. Oceanogr.*, **30**, 2535–2561. Find this article online

Hurlburt H. E., and J. D. Thompson, 1980: A numerical study of Loop Current intrusions and eddy-shedding. *J. Phys. Oceanogr.*, **10**, 1611–1651. Find this article online

Hurlburt H. E., and J. D. Thompson, 1982: The dynamics of the Loop Current and shed eddies in a numerical model of the Gulf of Mexico. *Hydrodynamics of Semi-Enclosed Seas*, J. C. J. Nihoul, Ed., Elsevier, 243–297.

Hurlburt H. E., and J. D. Thompson, 1984: Preliminary results from a numerical study of the New England Seamount Chain influence on the Gulf Stream. *Predictability of Fluid Motions*, G. Holloway and B. J. West, Eds., Amer. Inst. of Phys., 489–504.

Hurlburt H. E., and E. J. Metzger, 1998: Bifurcation of the Kuroshio Extension at the Shatsky Rise. *J. Geophys. Res.*, **103**, 7549–7566. Find this article online

Hurlburt H. E., and P. J. Hogan, 2000: Impact of 1/8° to 1/64° resolution on Gulf Stream model–data comparisons in basin-scale subtropical Atlantic Ocean models. *Dyn. Atmos. Oceans*, **32**, 283–329. Find this article online

Hurlburt H. E., A. J. Wallcraft, W. J. Schmitz Jr.,, P. J. Hogan, and E. J. Metzger, 1996: Dynamics of the Kuroshio/Oyashio current system using eddy-resolving models of the North Pacific Ocean. *J. Geophys. Res.*, **101**, 941–976. Find this article online

Levitus S., 1982: *Climatological Atlas of the World Ocean*. NOAA Prof. Paper 13, 173 pp. and 17 microfiche.

Metzger E. J., and H. E. Hurlburt, 1996: Coupled dynamics of the South China Sea, the Sulu Sea and the Pacific Ocean. *J. Geophys. Res.*, **101**, 12331–12352. Find this article online

Metzger E. J., H. E. Hurlburt, J. C. Kindle, Z. Sirkes, and J. Pringle, 1992: Hindcasting of wind-driven anomalies using a reduced-gravity global ocean model. *Mar. Technol. Soc. J.*, **26**, 23–32. Find this article online

Mitchell J. L., W. J. Teague, G. A. Jacobs, and H. E. Hurlburt, 1996: Kuroshio Extension dynamics from satellite altimetry and a model

simulation. *J. Geophys. Res.*, **101**, 1045–1058. Find this article online

Moore D. R., and A. J. Wallcraft, 1998: Formulation of the NRL Layered Ocean Model in spherical coordinates. NRL CR 7323-96-0005, 24 pp.

Moore M. I., and J. L. Wilkin, 1998: Variability in the South Pacific Deep Western Boundary Current from current meter observations and a high-resolution global model. *J. Geophys. Res.*, **103**, 5439–5457. Find this article online

Morey S. L., J. F. Shriver, and J. J. O'Brien, 1999: The effects of Halmahera on the Indonesian Throughflow. *J. Geophys. Res.*, **104**, 23281–23296. Find this article online

Munk W. H., 1950: On the wind driven ocean circulation. *J. Meteor.*, **7**, 79–93. Find this article online

National Oceanic and Atmospheric Administration,, 1986: ETOP05 digital relief of the surface of the earth. NGDC Data Announce 86-MGG-07, 7 pp.

Philips H. E., and S. R. Rintoul, 2000: Eddy variability and energetics from direct current measurements in the Antarctic Circumpolar Current south of Australia. *J. Phys. Oceanogr.*, **30**, 3050–3076. Find this article online

Rintoul S. R., and J. L. Bullister, 1999: A late winter hydrographic section from Tasmania to Antarctica. *Deep-Sea Res.*, **46A**, 1417–1454. Find this article online

Rochford P. A., J. C. Kindle, P. C. Gallagher, and R. A. Weller, 2000: Sensitivity of Arabian Sea mixed layers to 1994–1995 operational wind products. *J. Geophys. Res.*, **105**, 14141–14162. Find this article online

Salinger M. J., 1979: New Zealand climate: The temperature record, historical data and some agricultural implications. *Climatic Change*, **2**, 109–126. Find this article online

Semtner A. J., and R. M. Chervin, 1992: Ocean general circulation from a global eddy-resolving model. *J. Geophys. Res.*, **97**, 5493–5550. Find this article online

Shriver J. F., and H. E. Hurlburt, 1997: The contribution of the global thermohaline circulation to the Pacific to Indian Ocean throughflow via Indonesia. *J. Geophys. Res.*, **102**, 5491–5511. Find this article online

Stramma L., R. G. Peterson, and M. Tomczak, 1995: The South Pacific Current. *J. Phys. Oceanogr.*, **25**, 77–91. Find this article online

Sverdrup H. U., 1947: Wind-driven currents in the baroclinic ocean: With application to the equatorial currents of the eastern Pacific. *Proc. Natl. Acad. Sci. USA*, **33**, 318–326. Find this article online

Tilburg C. E., 2000: Ocean dynamics around New Zealand. Ph.D. thesis, The Florida State University, 106 pp. [Available from The Florida State University, Tallahassee, FL 32306].

Tilburg C. E., H. E. Hurlburt, J. J. O'Brien, and J. F. Shriver, 2001: The dynamics of the East Australian Current System: The Tasman front, the East Auckland Current, and the East Cape Current. *J. Phys. Oceanogr.*, **31**, 2917–2943. Find this article online

Uddstrom M. J., and N. A. Oien, 1999: On the use of high-resolution satellite data to describe the spatial and temporal variability of sea surface temperatures in the New Zealand region. *J. Geophys. Res.*, **104**, 20729–20751. Find this article online

Wallcraft A. J., 1991: The Navy Layered Ocean Model users guide. NRL (NOARL) Rep. 35, 21 pp.

Wallcraft A. J., and D. R. Moore, 1997: A scalable implementation of the NRL Layered Ocean Model. *Parallel Comput.*, **23**, 2227–2242. Find this article online

Warren B. A., 1973: Transpacific hydrographic sections at latitudes 43°S and 28°S: The SCORPIO Expedition-II. Deep water. *Deep-Sea Res.*, **20**, 9–38. Find this article online

Warren B. A., 1976: Structure of deep western boundary currents. *Deep-Sea Res.*, **23**, 129–142. Find this article online

Warren B. A., 1981: Deep circulation of the world ocean. *Evolution of Physical Oceanography*, B. A. Warren and C. Wunsch, Eds., MIT Press, 6–41.

APPENDIX

6. Explanation of Symbols and Notations

$$\frac{1}{a^2\cos^2\theta}\frac{\partial^2}{\partial\phi^2} + \frac{1}{a^2\cos\theta}\frac{\partial}{\partial\theta}\left(\frac{\partial}{\partial\theta}\cos\theta\right)$$

A Coefficient of isopycnal eddy viscosity

a Radius of the earth (6371 km)

C_b Coefficient of bottom friction

C_k Coefficient of interfacial friction

C_M Coefficient of additional interfacial friction associated with entrainment

$D(\Phi, \theta)$ Total depth of the ocean at rest

$$e_{\phi\phi_k} \qquad \frac{\partial}{\partial\phi}\left(\frac{u_k}{\cos\theta}\right) - \cos\theta\frac{\partial}{\partial\theta}\left(\frac{v_k}{\cos\theta}\right) = -e_{\theta\theta_k}$$

$$e_{\phi\theta_k} \qquad \frac{\partial}{\partial\phi}\left(\frac{v_k}{\cos\theta}\right) + \cos\theta\frac{\partial}{\partial\theta}\left(\frac{u_k}{\cos\theta}\right) = e_{\theta\phi_k}$$

$\mathbf{e}_k$ Angular deformation tensor

η_1 Deviation of free surface from its initial value

η_2 Deviation of the interface between two layers from its initial value

$$G_{kj} \qquad \begin{cases} g & \text{for } j \geq k \\ g - g(\rho_k - \rho_j)/\rho_0 & \text{for } j < k \end{cases}$$

f Coriolis parameter = $2\Omega \sin\theta$

g Acceleration due to gravity (9.8 m s^{-2})

h Local depth

h_k kth-layer thickness

h^+_k kth-layer thickness at which entrainment starts

h^-_k kth-layer thickness at which detrainment starts

Φ Longitude

ρ_0 Constant reference density

ρ_k kth-layer density, constant in space and time

$$\boldsymbol{\tau}_{\mathbf{k}} \qquad \begin{cases} \boldsymbol{\tau}_w & \text{for } k = 0 \\ C_k\rho_0|\mathbf{v}_k - \mathbf{v}_{k+1}|(\mathbf{v}_k - \mathbf{v}_{k+1}) & \\ & \text{for } k = 1, \ldots, n-1 \\ C_b\rho_0|\mathbf{v}_n|\mathbf{v}_n & \text{for } k = n \end{cases}$$

$\boldsymbol{\tau}_w$ Wind stress

t Time

θ Latitude

$\mathbf{v}_{gk}$ Geostrophic velocity in layer k

$\mathbf{V}_k$ $h_k\mathbf{v}_k = \mathbf{e}_\phi U_k + \mathbf{e}_\theta V_k$

$\mathbf{v}_k$ kth-layer velocity = $\mathbf{e}_\phi u_k + \mathbf{e}_\theta v_k$

Ω Angular rotation rate of the earth ($7.292\ \ 205 \times 10^{-5}\ \mathrm{s}^{-1}$)

ω_k
$$\begin{cases} 0 & \text{for } k = 0, n \\ \omega_k^+ - \omega_k^- - W_k\hat{\omega}_k & \\ & \text{for } k = 1, \ldots, n-1 \end{cases}$$

ω^+_k $\tilde{\omega}_k[\max(0, h^+_k - h_k)/h^+_k]^2$

ω^-_k $\tilde{\omega}_k[\max(0, h_k - h^-_k)/h^+_k]^2$

$\hat{\omega}_k$ $(\overline{\omega^+}_{\overline{k}} - \overline{\omega^-}_{\overline{k}})/\overline{W}_{\overline{k}}$

$\tilde{\omega}_k$ kth interface reference diapycnal mixing velocity

$W_k(\phi, \theta)$ kth interface weighting factor for global diapycnal mixing designed to conserve mass within a layer in compensation for explicit diapycnal mixing due to $h_k < h^+_k$ (i.e., $\omega^+_k - \omega^-_k$), and net transport through the lateral boundaries of layer k.

Tables

Table 1. World Ocean simulations

Expt	A ($\mathrm{m^2\ s^{-1}}$)	Initial layer thickness (m)	Wind forcing	Model years spanned	Comments
RG	100	250/=	Seasonal*	250–325	Linear, reduced-gravity global simulation
FB	100	155/185/210/225/255/5500	Seasonal*	282–299	Flat-bottom global simulation
RBa	100	153/185/260/375/525/variable	Seasonal*	860–975	Realistic-bottom-topography global simulation
RBb	500	300/variable	None	0–180	Two-layer idealized regional simulation

Click on thumbnail for full-sized image.

Table 2. Additional model parameters

Parameters	Value	Simulations	Definition
α	Not applicable 0 0.65 1.0	RG FB RBa RBb	Multiplier for topographic amplitude with respect to 6500 m
σ_k	25.45/27.55 25.24/26.47/26.99/27.23/27.39/27.77 25.25/26.59/27.03/27.30/27.53/27.77 26.00/27.60	RG FB RBa RBb	Density of layer k
$\Delta\theta$	1.0° 1/2°	RG, FG, RBa RBb	Latitudinal grid resolution
$\Delta\phi$	45/256° 45/64°	RG, FB, RBa RBb	Longitudinal grid resolution

Click on thumbnail for full-sized image.

Figures

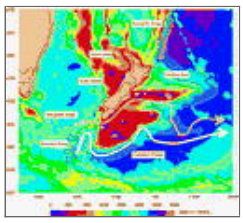

Click on thumbnail for full-sized image.

FIG. 1. Seafloor topography (m) surrounding New Zealand and schematic diagram of the Southern Hemisphere subtropical front (gray line), the subantarctic front (white line), and the Deep Western Boundary Current (transparent line). The locations of the

fronts are based on SST observations (Uddstrom and Oien 1999) and simulations from this numerical study. The location of the DWBC is based on a similar figure by Carter and Wilkin (1999)

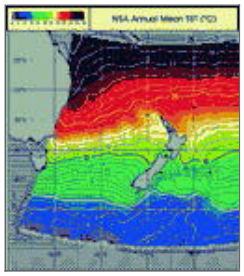

Click on thumbnail for full-sized image.

FIG. 2. Annual mean of sea surface temperature (°C) computed over 5 yr, Jan 1993–Dec 1997, compiled by Uddstrom and Oien (1999). The path of the SAF generally follows the 8°–8.5°C isotherms. The STF is more complex. It is associated with the 12°–13° C isotherms west and the 11°–13°C isotherms directly east of New Zealand, but its southward dip near 53°S, 173°W is evident in the slightly colder 9°–9.5°C isotherms

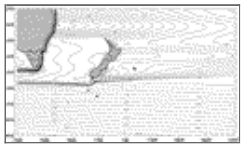

Click on thumbnail for full-sized image.

FIG. 3. Mean sea surface height deviations (cm) from the 1½-layer reduced-gravity simulation, RG. Note the contour interval changes from 5 to 50 cm south of New Zealand. The linear simulation contains extremely highly transport within the Southern Ocean. Note the western boundary current corresponding to the Southland Current is *southward*, not northward as observed

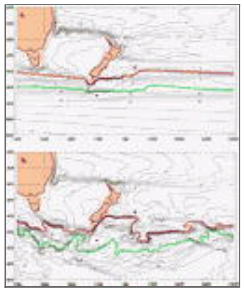

Click on thumbnail for full-sized image.

FIG. 4. Mean sea surface height deviations (cm, contour interval is 5 cm) from (a) the flat-bottom simulation (FB) and (b) the realistic-bottom-topography simulation (RBa). Sea surface deviation contours that are representative of the STF (red line) and SAF (green line) are highlighted. Note the similarities in the far field (i.e., both simulations exhibit strong zonal flow at ~ 34° and ~ 47°S). However, RBa produces a realistic STF and SAF and FB does not. Note the southward dip in the STF at 53°S, 173°W corresponding to the 9°–9.5°C isotherms in the observations

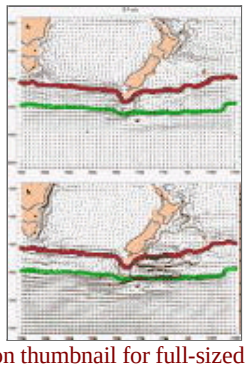

Click on thumbnail for full-sized image.

FIG. 5. (a) Location of the STF (red line) and SAF (green line) superimposed on the mean surface currents (m s^{-1}) from FB. The highlighted fronts are identical to those in Fig. 4a. Note the nearly zonal flow associated with the two fronts. (b) Location of the STF (red line) and SAF (green line) superimposed on the mean abyssal currents (m s^{-1}) from FB. Note the lack of a DWBC southeast of New Zealand

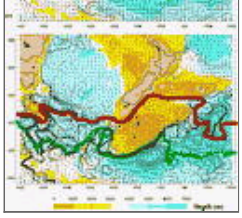

Click on thumbnail for full-sized image.

FIG. 6. (a) Mean surface currents (m s^{-1}) and location of the STF (red line) and SAF (green line) from RBa superimposed on bottom topography (m). The highlighted fronts are identical to those from Fig. 4b. The position of the simulated STF is coincident with a strong Southland Current flowing northeastward along the coast of South Island, a zonal flow south of Chatham Rise, and a return to the original latitude at ~ 172°W. The position of the simulated SAF is coincident with the surface flow along the southern edge of the Campbell Plateau. (b) Location of the simulated STF (red line) and SAF (green line) from RBa superimposed on the mean abyssal currents (m s^{-1}) and bottom topography (m). Note the lack of an abyssal current underneath the Southland Current but a strong DWBC along the eastern edge of the Campbell Plateau

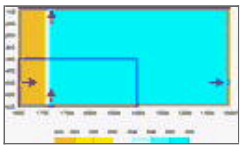

Click on thumbnail for full-sized image.

FIG. 7. Domain and bottom topography (color in meters) of the two-layer experiment, RBb. The red arrows represent flow through ports in the lower layer, simulating the DWBC. The blue arrows represent flow through ports in the upper layer, simulating flow associated with the STF. The blue rectangular outline represents the region displayed in Fig. 8

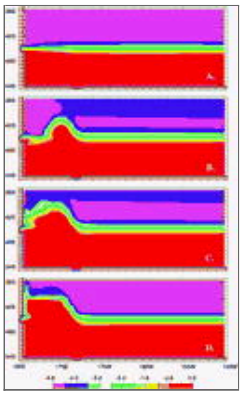

Click on thumbnail for full-sized image.

FIG. 8. Surface transport streamfunctions (1 Sv $\equiv 10^6$ m^3 s^{-1}, contour interval is 0.4 Sv) from the two-layer simulation RBb at (a) T = 0 yr (no abyssal flow), (b) T = 3 yr (note the initial advection of the streamfunctions), (c) T = 7 yr (note the westward propagation of the stream functions), and (d) T = 80 yr (note the formation of a western boundary current solely due to a topographically constrained DWBC)

* Naval Research Laboratory Contribution Number NRL/JA/7320/01/0006.

+ Current affiliation: Physical Ocean Science and Engineering Program, Graduate College of Marine Studies, University of Delaware, Newark, Delaware

Corresponding author address: Charles E. Tilburg, Graduate College of Marine Studies, University of Delaware, 102 Robinson Hall, Newark, DE 19716.E-mail: tilburg@udel.edu

top